A Coverage Self-Consistent Microkinetic Model for Vapor-Phase Formic Acid Decomposition over Pd/C Catalysts

Saurabh Bhandari[a], Srinivas Rangarajan [a,1], Sha Li [a,2], Jessica Scaranto[a], Suyash Singh[a], Christos T. Maravelias [a,3], James A. Dumesic[a], Manos Mavrikakis[a]*

[a]*Department of Chemical and Biological Engineering, University of Wisconsin-Madison, Madison, WI 53706, USA*

* Corresponding author: emavrikakis@wisc.edu

Present Address:

[1]*Department of Chemical & Biomolecular Engineering, Lehigh University, Bethlehem, PA 18015*

[2]*Chemistry and Chemical Engineering Guangdong Laboratory, Shantou, Guangdong, China 515041*

[3]*Department of Chemical and Biological Engineering, Princeton University, NJ 08540*

ABSTRACT

An iterative approach utilizing density functional theory (DFT, PW91-GGA)-informed mean-field microkinetic models and reaction kinetics experiments is used to determine the reaction mechanism and the active site for formic acid (HCOOH, FA) decomposition over a Pd/C catalyst. Models parameterized using DFT energetics on clean Pd(100) and Pd(111) required large corrections to the DFT energetics for capturing our experimental data. Further, both Pd(111) and Pd(100) models predicted a high coverage of adsorbed CO (CO*), inconsistent with the assumption of a clean surface at which the rate parameters for these models were calculated. To better represent the active site under reaction conditions and explicitly account for the presence of CO*, subsequent microkinetic models were formulated using DFT energetics that were calculated

on partially (5/9 ML) CO*-covered Pd (111) and (100) facets. Upon parameter adjustment, the resultant 5/9 ML CO*-covered Pd(100) model, although consistent in terms of CO* coverage, was unable to capture the dehydration path measured in the experiments, and was therefore deemed not to offer an accurate representation of the active site for FA decomposition over Pd/C. In contrast, a partially CO*-covered Pd(111) model was better representing the catalytic active site, as in addition to being consistent in terms of CO* coverages, required small adjustments of the DFT parameters to accurately capture the experimental dataset (both dehydrogenation and dehydration). Our results suggest that the reaction occurs via the spectroscopically elusive carboxyl (COOH*) intermediate and that spectator CO*-assisted decomposition pathways play an important role under typical experimental conditions. Further, our study highlights the importance of striving for coverage self-consistent microkinetic models and for including spectator-assisted mechanisms in order to develop an improved picture of the active site under reaction conditions.

1. INTRODUCTION

Transition towards a sustainable energy future strongly depends on the effective deployment of renewable energy carriers. Obtained as a byproduct of biomass reforming,[1-3] formic acid (HCOOH, FA) has been widely considered as one of the most promising hydrogen storage vectors.[4-10] Its high volumetric capacity (53.4 g-H_2/l), low toxicity, and low flammability, makes FA a promising carbon-neutral hydrogen carrier for transportation applications. FA can be used as a fuel in direct formic acid fuel cells (DFAFCs)[11-16] or alternatively, it can be decomposed to generate on-board hydrogen for powering hydrogen fuel cells, a technology which is in more advanced stages. Importantly, FA has also been explored as an *in situ* hydrogen source for hydrogenation reactions.[17-26] Due to FA's potential as a hydrogen carrier molecule, FA

decomposition has been widely investigated in the heterogeneous catalysis literature over a variety of catalysts including metals,[27-30] metal oxides,[31-34] and metal carbides.[35, 36]

FA decomposition can occur through the dehydrogenation reaction to form CO_2 and H_2 (ΔH^o = -14.9 kJ/mol) and through the dehydration reaction to form CO and H_2O (ΔH^o = 26.2 kJ/mol), the two routes coupled together through the water gas shift reaction (WGSR).[37, 38] Pt-group metals, especially Pd and Pt, have been reported to be the most active monometallic catalysts in terms of FA decomposition selectivity towards H_2 (>95%).[39, 40] In the 1960s, Sachtler and Fahrenfort proposed a volcano-type relationship correlating the FA decomposition temperature at fixed conversion with the heat of formation of bulk metal formate and identified Pt-group metals near the peak.[41] Recent experimental studies by Tang *et al.*[42] on unsupported metal powder catalysts (decreasing turnover frequency: Pt > Cu > Pd > Rh > Ni) and by Solymosi *et al.*[43] on carbon-supported metal catalysts (decreasing specific activity: Ir ~ Pt ~ Pd > Ru > Rh), have also demonstrated Pd as one of the most active monometallic catalysts for FA decomposition.

Despite numerous experimental and theoretical studies involving Pd-based catalysts, detailed mechanistic understanding of the reaction mechanism, dominant reaction pathways, surface intermediate(s), and the active site(s) remains largely unsettled. Li *et al.*[44] reported that the apparent activation energy barrier for FA decomposition is independent of the particle size of Pd/C and suggested the reaction to be structure insensitive. They additionally reported an inverse dependence of the turnover frequency (TOF) on the size of the catalyst particles. These observations are in disagreement with a previous study by Garcia *et al.* who reported a volcano-type dependence of the TOF with the particle size and instead suggest the reaction to be structure sensitive.[45] Additionally, the nature of the key reactive intermediate is still under debate. While certain *in situ* spectroscopic studies have corroborated the presence of formate (HCOO*) on Pd

catalysts, the experimental selectivity of FA towards CO suggests the participation of the spectroscopically elusive carboxyl (COOH*) species in the reaction mechanism.[37, 38, 46] Accordingly, a mechanistic model that comprehensively captures experimental kinetics, over a wide range of experimental conditions, could contribute to resolving open questions and enable the elucidation of the reaction mechanism and of the active site for FA decomposition over Pd catalysts.

In this study, we combine DFT-informed microkinetic models and reaction kinetics experiments to iteratively develop a coverage self-consistent description of the active site[47] for FA decomposition on Pd/C. Our goal of coverage self-consistency strives to reconcile coverages of surface intermediates as predicted by the microkinetic model with those utilized in the DFT calculations informing the microkinetic model,[48-53] an agreement that is often-ignored in typical microkinetic modeling based analyses. Upon parameter estimation to fit with reaction kinetics experiments, the microkinetic models based on DFT-energetics derived on clean Pd(111) and Pd(100) pointed to a high CO* coverage (~0.90 ML and ~0.99 ML for Pd(111) and Pd(100), respectively) under reaction conditions. These coverages were inconsistent with the starting assumption of a clean surface used in the initial DFT calculations. Therefore, subsequent microkinetic models were parameterized with DFT energetics calculated on partially (5/9 ML) CO*-covered Pd surfaces, with explicit dependence of the thermochemistry and kinetics of the reaction network on the CO* coverage. The resultant "*CO* coverage cognizant*" microkinetic models in addition to being self-consistent in CO* coverage, also provided quantitative agreement with the reaction kinetics experiments, after reasonable parameter adjustments. Our approach highlights the importance of investigating reaction networks under realistic catalytic surface environment, in terms of the coverages of spectator species, for obtaining accurate initial estimates

of the kinetic and thermodynamic rate-parameters. Importantly, we also demonstrate that the presence of spectator species (e.g.: CO*) can alter the reaction mechanism by enabling spectator-assisted reaction pathways to play a crucial role under reaction conditions. We provide detailed insights on the reaction mechanism, the nature of the active site ((111) versus (100)), the rate-controlling steps, and the decoration of the active site under reaction conditions.

2. METHODS

2.1 Experimental Section

Reaction Kinetics Experiments

The reactor setup and experimental protocols were similar to those used in our previous studies.[48, 51] The reaction kinetics experiments were performed using a 12.7 mm (outer diameter) stainless steel reactor, operated in a fixed-bed down-flow configuration. In a typical experiment, ca. 60 mg (dry weight) of 1 wt.% Pd/C catalyst (Sigma Aldrich) was charged into the reactor and packed in place using silica chips. The temperature of the reactor was measured using a K-type thermocouple and was modulated by a furnace connected to a variable autotransformer. Prior to the reactivity measurements, the catalyst was reduced *in situ* at 573 K (ramp rate of 1 K min^{-1}) under 25% H_2/He (60 cm^3 min^{-1}) for 4h and cooled down to the reaction temperature under He flow, ensuring the presence of the Pd metallic state and the absence of a Pd-hydride phase.[54] Further, under steady-state reactivity measurements the H_2 partial pressure is sufficiently low (<2.5E-3 atm) to prevent formation of hydride phases.[55] Thus, hydride formation was determined to be irrelevant under our experimental conditions.

The experiments were performed at a total pressure of 1 atm. The partial pressures of gases were controlled at the reactor inlet using calibrated mass flow controllers. The mole percentage of reactants in the gas-phase was maintained between 1-5% (partial pressure range of 0.01-0.05 atm)

for FA, 0-10% (partial pressure range of 0-0.10 atm) for dehydrogenation products (H_2 and CO_2), and 0-0.1% (partial pressure range of $0\text{-}10^{-3}$ atm) for dehydration products (H_2O and CO), with He as the balance gas. FA was introduced in the reactor system as a liquid using a syringe pump (Chemyx Inc.), evaporated at the reactor inlet and was carried through the reactor with He flow. The reactor effluent was passed through a condenser to remove the unconverted FA from the gas stream. The composition of the residual effluent stream was analyzed through a gas chromatograph with a thermal conductivity detector (GC-TCD, Shimadzu), fitted with AllTech HayeSep DB 100/120 (30' x 1/8" x .085" SS) column. The reactor effluent was passed through a condenser (ethylene glycol/dry ice bath; maintained below -30 ºC) to remove unconverted FA and water from the gas stream, which was essential for preventing FA-induced degradation of the separation media in the GC column. At steady state, the composition of decomposition products – CO_2 and CO were used to determine the reaction rate corresponding to FA dehydrogenation and dehydration, respectively.[28, 39, 40, 51] For the GC-TCD method employed in our experiments, the detection limit for both CO_2 and CO species was c.a. 1 ppm. To ensure reproducibility of our experiments, the reported reaction rates were quantified by averaging from five distinct sample injections (resulting in standard deviations of <5% error). The carbon balance was verified by measuring the condensed FA and the decomposition products CO/CO_2 and was determined to be within 99-99.5%. The conversion was calculated based on the number of moles of FA converted to the decomposition products ($CO_2 + H_2$ and $CO + H_2O$). To gather experimental data in a kinetically limited regime, the reactor was operated at differential conversion (below 10% conversion, for all but one data point) (Supporting Information – **Table S1**).

The apparent activation energy barriers for the dehydrogenation and dehydration reactions were measured by varying the temperature from 353 to 393 K. The apparent reaction orders for the

dehydrogenation and dehydration reactions with respect to the reactant – FA, dehydrogenation products – CO_2 and H_2, and dehydration products – CO and H_2O, were determined by varying the partial pressure of the respective component in the feed stream, at a total pressure of 1 atm and reaction temperature of 373 K.

Catalyst Characterization

The surface site density for the Pd/C catalyst sample was determined by performing CO chemisorption at 298 K.[56] Prior to CO chemisorption, the catalyst sample was reduced using the same protocols followed during the reaction kinetics experiments, as described above. The Pd surface site density was obtained using a surface stoichiometry of 3:2 for surface Pd atom:CO.[49, 57] The TOFs for the dehydrogenation and dehydration reactions are reported with respect to the surface site-density of the Pd/C catalyst.

The morphology of the supported Pd/C catalyst was characterized using a scanning transmission electron microscope (FEI-Titan STEM) with aberration correction (spatial resolution of <0.1 nm), operated at 200 kV. The images were collected in high-angle annular dark field (HAADF) mode with detector angle ranging from 54 to 270 mrad, probe convergence angle of 24.5 mrad, and probe current of approximately 25 pA. The samples were charged into the microscope through a procedure described previously.[51] The particle size distribution was determined by analyzing the STEM micrographs using the ImageJ software. The average particle size was determined by sum normalizing the particle diameters of the analyzed Pd/C catalyst (Supporting Information – **Figure S1**). Approximately 1400 particles, from different regions in the catalyst sample, were analyzed to determine the particle size distribution.

2.2 Microkinetic Model

Reaction Network

Our reaction network comprised of 5 gas-phase species, 12 surface species, and 26 elementary steps (**Scheme 1**). Elementary steps 1-5 represent the adsorption and desorption of the reactant and products, respectively. Steps 6-7 and 8-10 represent the formation of dehydrogenation product – CO_2 – through the direct decomposition of formate (HCOO*) and carboxyl (COOH*) intermediate, respectively. The formation of dehydration product, CO, through the dehydroxylation of COOH* is indicated by steps 11-13. Steps 14-16 describe the reactions common with the redox mechanism in the WGSR.[37, 38] Elementary reactions involving CO-/OH-/O-assisted decomposition routes are described by steps 17-26.

We calculate the energetics of the reaction network using DFT (GGA-PW91[58]; DACAPO[59, 60]) on clean and on partially CO*-covered Pd(100) and Pd(111) model surfaces (Supporting Information – **Section S3**). A comprehensive discussion of the DFT results was presented in a recent study.[61] In this work, we utilize the DFT energetics to obtain initial estimates of the thermodynamic and kinetic rate parameters and formulate mean-field microkinetic models.

Reaction Network for Formic Acid (FA) Decomposition

Adsorption/Desorption

1. $HCOOH(g) + * \leftrightarrow HCOOH*$
2. $CO_2* \leftrightarrow CO_2(g) + *$
3. $CO* \leftrightarrow CO(g) + *$
4. $H_2O* \leftrightarrow H_2O(g) + *$
5. $2H* \leftrightarrow H_2(g) + 2*$

Dehydrogenation

6. $HCOOH* + 2* \leftrightarrow HCOO* + H*$
7. $HCOO* \leftrightarrow CO_2* + H*$
8. $HCOOH* \leftrightarrow HCOOHpa*$
9. $HCOOHpa* + * \leftrightarrow COOH* + H*$
10. $COOH* + * \leftrightarrow CO_2* + H*$

Dehydration

11. $COOH* \leftrightarrow cis\text{-}COOH*$
12. $cis\text{-}COOH* + * \leftrightarrow CO* + OH*$
13. $OH* + H* \leftrightarrow H_2O* + *$

Redox

14. $2OH* + * \leftrightarrow H_2O* + O*$
15. $OH* + * \leftrightarrow O* + H*$
16. $CO* + O* \leftrightarrow CO_2* + *$

Spectator-Assisted

17. $HCOOH* + CO* + * \leftrightarrow HCOO* + COH*$
18. $HCOO* + CO* \leftrightarrow CO_2* + COH* + *$
19. $COOH* + CO* \leftrightarrow CO_2* + COH*$
20. $COH* + CO* \leftrightarrow CO* + HCO*$
21. $COH* \leftrightarrow CO* + H*$
22. $HCO* \leftrightarrow CO* + H*$
23. $HCO* + O* \leftrightarrow CO* + OH*$
24. $COH* + O* \leftrightarrow CO* + OH*$
25. $HCOO* + OH* \leftrightarrow CO_2* + H* + OH*$
26. $HCOO* + H_2O* \leftrightarrow CO_2* + H* + H_2O*$

Scheme 1 Reaction network considered for formic acid (FA) decomposition as investigated by Li *et al*.[61] Surface sites are denoted by '*'; adsorbed reaction intermediates are denoted by a subscript '*' (e.g., HCOOH*, HCOO*, COOH*, etc.).

Model Formulation

Given the low per pass conversion in our reaction kinetics experiments (<10%, for all but one data point), we modeled the reactor as a continuous stirred tank reactor (CSTR).[51] Entropy values corresponding to the adsorbed intermediates and transition states were calculated using the DFT-derived vibrational frequencies. Shomate parameters were fit using DFT-derived vibrational frequency calculations and statistical mechanics,[62] which were used to incorporate zero-point energy (ZPE) corrected and temperature-dependent thermochemistry and kinetics in our models.

Parameter estimation was performed using the generic sequential optimization framework developed by Rangarajan et al.[63] The optimization objective (**Equation 1**) consisted of a least-squares representation of model-experiment mismatch corresponding to dehydrogenation and

dehydration TOFs for all experimental conditions 'c', along with a term penalizing (δ = 0.05) the corrections from the DFT-derived energetics to obtain sparse solutions. By minimizing the objective function value (**Equation 1**), we search for corrections (π-π_{DFT}; vector comprising all parameter adjustments) in sensitive parameters that are required to fit model-predictions (y) with the experimental measured dehydrogenation and dehydration TOFs ($\overline{y}$).

$$Z_{Param.Est} = Min\left[\sum_{c\in C}\left(1-\frac{\overline{y_c}}{y_c}\right)^T\left(1-\frac{\overline{y_c}}{y_c}\right)\right] + \delta(\pi-\pi_{DFT})^T(\pi-\pi_{DFT}) \quad (1)$$

To elucidate plausible alternate solutions, we employed a multi-start approach using Latin hypercube sampling to randomly initialize the starting values of the corrections to the DFT parameters (binding and transition state energies) from which the optimization is initiated.[63] We searched for favorable solutions in a ±0.6 eV range from the DFT-derived binding and transition-state energy values. A positive correction to the binding energy indicates destabilization of the corresponding reaction intermediate vs. the DFT-computed value, while negative correction to the binding energy indicates stabilization vs. the DFT-computed value.

Gas-phase reaction energetics were calculated using Shomate parameters for both dehydrogenation and dehydration pathways and were compared with the corresponding values obtained from NIST.[64] By adjusting the CO(g) gas-phase energy by -0.60 eV, we were able to achieve good agreement with the NIST reaction energetics. The adjusted CO(g) gas-phase energy is used in our microkinetic models. While discussing the corrections for adsorbed CO*, we explicitly specify if: (1) the correction refers to that determined using parameter estimation (i.e, correction in the energy of adsorbed CO* only) or (2) the correction refers to the 'overall' correction in the binding energy of CO* (i.e., considering the corrections for both adsorbed CO*

and gas-phase CO(g)). The kinetic and thermochemistry parameters used in our models are included in **Section S3** of the Supporting Information.

We utilized a mean-field implementation to account for spectator CO* coverage-effects.[37, 51, 65] By investigating the reaction network at varying levels of CO* coverage, we derived polynomial functions for the binding energies (BE) and transition-state (TS) energies dependent on surface coverage of CO*. The binding energy of reaction intermediates was evaluated at different levels of spectator CO* coverages, varying from clean surface (i.e., no coadsorbed CO*) to 5/9 ML of spectator CO* in increments of 1/9 ML of CO*. The transition state energies were evaluated on clean and 5/9 ML CO* covered facets. At every investigated CO* coverage level, we rigorously generated CO* co-adsorbed configurations, without apriori assuming: (1) the preferred adsorption sites for the CO* molecules or (2) the relative arrangement of CO* species wrt. the adsorbate under consideration or other spectator species. For each coverage level c.a. 15-20 structures were generated as initial guesses and each one of them was optimized using DFT calculations. The DFT-derived energetics for each of the converged structures was used to determine the most stable co-adsorbed configuration. These structures were ultimately used for computing the differential binding energy of reaction intermediates. To determine the most stable transition state energy, for every elementary step, nudged elastic band (NEB) calculations were initialized using several initial states, wherein the reaction intermediate is decorated by the relevant coverage of CO* spectators. Each of these calculations were explicitly converged and the respective transition state structure was verified by performing vibrational frequency analysis, yielding a single imaginary frequency along the reaction coordinate. The lowest energy structure among the obtained structures was defined as the transition state for a given elementary step. We refer the interested reader to our previous work for additional details, including atomic scale representation of the most stable

binding and transition state structures on clean and partially CO*-covered (100) and (111) facets.[61] The energetics used in the microkinetic models were updated on-the-fly per the CO* coverages determined during the model simulation, thereby ensuring the use of CO* coverage-cognizant energetics.[51]

Further, we used the optimized CO* coverage-dependent energetics to simulate a plug-flow reactor (PFR) and verified the applicability of a controlled-stirred tank reactor (CSTR) model. The results from the PFR simulation demonstrated that CO* coverages saturate rapidly (to within 10% of steady-state CSTR coverages) in the initial portion of the reactor (~2% of normalized bed-length), which reinforces the choice of CSTR for performing parameter estimation and for modeling the kinetics of FA decomposition on Pd/C (Supporting Information – **Section S5**).

3. RESULTS AND DISCUSSION

Reaction Kinetics Experimental Results

The apparent activation energy barriers for the dehydrogenation and dehydration pathways were measured in a temperature range of 353-393K. The activation energy barrier for the dehydrogenation pathway was determined to be 69.0 kJ/mol (**Figure 1**), which were in agreement with the values (65-67 kJ/mol) reported in the literature for Pd/C catalysts.[28, 40] The apparent activation energy barrier for the dehydration pathway was determined to be 82.9 kJ/mol (**Figure 1**). The selectivity towards dehydrogenation pathway had a moderate temperature dependence, decreasing from 99.5% at 353 K to 98.9% at 393 K.

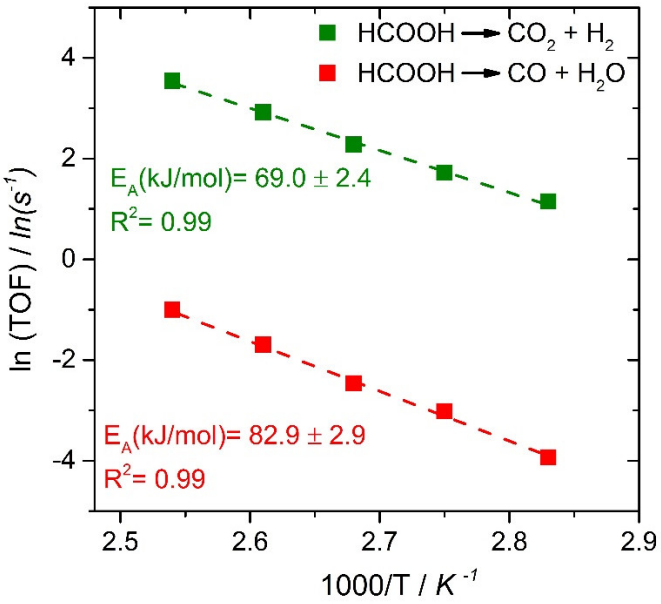

Figure 1 Arrhenius plot for FA dehydrogenation: HCOOH ↔ CO_2 + H_2 (green) and dehydration: HCOOH ↔ CO + H_2O (red) on Pd/C at 1 atm. The dashed lines represent the fit to the experimentally determined TOFs.

In a FA partial pressure range of 1-5%, we determined reaction orders with respect to FA of -0.03 and 0.08 for dehydrogenation and dehydration, respectively. Co-feeding the dehydration product CO had a strong poisoning effect on the FA decomposition reaction. Severe deactivation of Pd catalysts due to CO site blocking is well known and has been observed for both vapor- and liquid-phase FA decomposition.[27, 28, 40, 66, 67] CO partial pressure of 0.02% at 373 K, led to a 4-fold decrease in the dehydrogenation TOF compared with when no CO was co-fed (from 0.16 s^{-1} to 0.04 s^{-1}) (Supporting Information – **Table S1**). The reaction order with respect to CO was determined as -0.58 for the dehydrogenation pathway. The dehydration reaction order for the CO-cofeed experiments could not be accurately quantified due to small selectivity of Pd/C towards CO formation.

The reaction order with respect to H_2 was determined to be -0.26 for the dehydrogenation reaction pathway and 0.02 for the dehydration pathway. The partial pressure of decomposition product CO_2 incurred no appreciable change in the TOFs of either reaction pathway. We observed a zero-reaction order with respect to CO_2 for the dehydrogenation pathway and a small positive order (0.11) for the dehydration reaction.

We determined a zero-reaction order with respect to H_2O for both dehydrogenation (0.02) and dehydration (0.04). Negligible improvement towards the dehydrogenation selectivity indicates absence of water-gas shift reaction under our experimental conditions, which is in agreement with previous experimental studies on Pd/C catalysts.[28]

Microkinetic Modeling Results

The models formulated using DFT-derived energetics calculated on clean Pd(100) and Pd(111) surfaces predicted reaction rates that were several orders of magnitude smaller than the experimentally measured rates. Accordingly, we performed parameter estimation to identify the corrections to the DFT energetics that would yield quantitative agreement with the experimentally determined TOFs. The results obtained from the optimized (i.e., parameter-adjusted) clean Pd(100) and clean Pd(111) solutions were as follows: (1) Both models failed to accurately predict the dehydrogenation reaction rates for the CO co-feed subset (0.02-0.1% CO, 2.6% FA, 373 K) of the experimental dataset. Under these conditions, both models significantly underpredicted the dehydrogenation TOFs compared with those determined experimentally. (2) Both models required large corrections of >0.3 eV for several parameters, which were outside the commonly accepted error of ~0.2 eV for DFT-GGA.[68, 69] (3) Averaged over the experimental conditions, both models predicted high surface coverage of CO* (~0.99 ML and ~0.90 ML for Pd(100) and Pd(111), respectively) which was inconsistent with the assumption of a clean surface at which the DFT

energetics for these models were calculated at. The models were therefore inconsistent in terms of the surface coverages. Since the clean Pd(100) and clean Pd(111) solutions failed on the three counts noted above, we conclude that these models do not accurately capture the nature of the active site and its surface environment under reaction conditions. The results from clean surface models are discussed in further detail in **Section S2** of the Supporting Information.

Motivated by the evidence of CO* on the surface of the catalyst under FA decomposition reaction conditions,[70-72] together with the results obtained from the clean-surface microkinetic models, we performed new DFT calculations on partially (5/9 ML) CO*-covered Pd(100) and Pd(111) (detailed in a separate article[61]). Subsequently, CO* coverage-cognizant microkinetic models were formulated for both Pd(100) and Pd(111), with explicit consideration of the variation in binding and transition-state energies on CO* coverage. Both models predicted reaction rates that were several orders of magnitude smaller than the experimentally observed rates. We therefore performed parameter estimation to adjust the energetics and improve parity with the experiments. We note that the CO*-spectator coverage of 5/9 ML was used only as an initial estimate of the *in situ* CO* coverage. In case the microkinetic model predictions for the surface coverages were drastically different from those utilized herein, we would have re-evaluated the reaction network in the presence of suitable coverages of the relevant reaction intermediate(s). The solutions that resulted from parameter estimation for the CO* coverage-cognizant Pd(100) and Pd(111) models are presented below:

CO* Coverage-Cognizant Pd(100) Model

Upon parameter estimation, the microkinetic model formulated using DFT energetics derived on 5/9 ML CO*-covered Pd(100)[61] failed to fit our experimental dataset in a satisfactory manner. First, the Pd(100) solution was completely selective towards dehydrogenation; i.e., the model

failed to predict any flux through the dehydration pathway (**Figure 2** (b)). This was in contrast with our experimental measurements, wherein we determined both dehydrogenation and dehydration to be active on Pd/C, with ~99% selectivity towards dehydrogenation. Second, under CO co-feed conditions (0.02-0.1% CO, 2.6 % FA, 373 K), the model predicted a complete shutdown of the dehydrogenation reaction (**Figure 2** (a) – inset), whereas experimentally we determined the reaction to be active, although the TOFs were reduced by factor of 4-10, compared to those under baseline conditions (2.6% FA, 373 K).

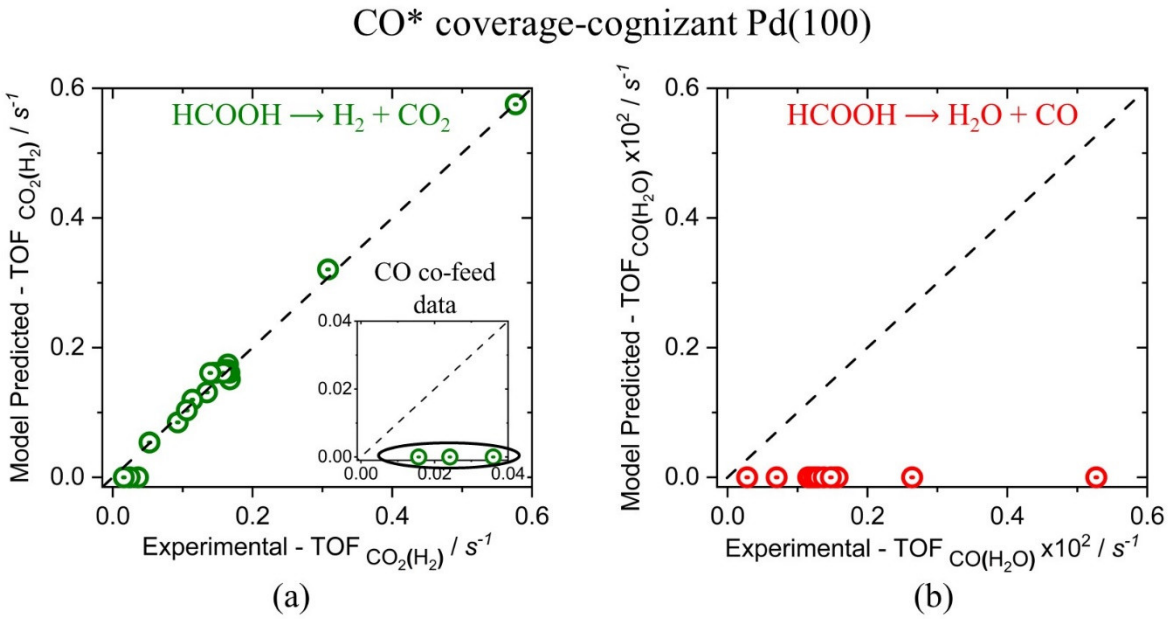

Figure 2 Parity plot of CO* coverage cognizant Pd(100) model predicted vs. experimental TOFs (s^{-1}) for (a) Dehydrogenation: HCOOH ↔ CO_2 + H_2; inset shows the parity at low TOFs (corresponding to CO co-feed experiments), (b) Dehydration: HCOOH ↔ CO + H_2O.

On Pd(100), the reaction occurs through the formate mechanism (HCOOH* ↔ HCOO* + H* ↔ CO_2* + 2H* ↔ CO_2 + H_2). Our model predicted no flux through the carboxyl (COOH*) mechanism under our reaction conditions. Since carboxyl is a precursor for CO formation, the lack

of carboxyl participation in the reaction mechanism under steady-state catalytic conditions, resulted in no reaction flux going through the dehydration pathway on partially CO*-covered Pd(100).

Parameter estimation led to a stabilization in the BE of HCOO* by 0.16 eV (**Table 1**). The BE of H* and CO* required corrections of +0.16 eV and +0.19 eV, respectively. Parameter estimation required three corrections to activation energy barriers, all of which were within the PW91-GGA error. The activation energy barriers for HCOO* formation (HCOOH* + 2* ↔ HCOO* + H*) and HCOO* decomposition (HCOO* ↔ CO_2* + H*) required corrections of –0.08 eV and –0.10 eV, respectively. The H-H recombinative desorption step to form H_2(g) required a correction of +0.14 eV.

Table 1 Corrections to the DFT-derived binding energy of reaction intermediates and activation energy barrier of the elementary steps for the CO* coverage cognizant Pd(100) model, as obtained from parameter estimation. †For CO*, the number outside the parenthesis refers to the correction in the energy of CO* as predicted from parameter estimation, while the number within the parenthesis ([•]) represents the 'overall' correction in the binding energy of CO*, which also includes the adjustment to the CO(g) gas-phase energy by -0.60 eV (see Section 2.2 – Model Formulation).

5/9 ML CO-covered Pd(100)*	*Corrections / eV*
Intermediate	*ΔBE*
HCOO*	-0.16
CO*	-0.41 [+0.19]†
H*	+0.16
Elementary Step	ΔE_A
HCOOH* + 2* ↔ HCOO* + H*	-0.08
HCOO* ↔ CO_2* + H*	-0.10
2H* ↔ H_2(g) + 2*	+0.14

Averaged over the experimental conditions, the model predicted surface coverages of 0.44 ML CO*, 0.06 ML H*, and 0.50 ML vacant sites (**Figure 3**). Consistent with the assumption of a 5/9 ML CO*-covered Pd(100) at which DFT energetics were calculated at, this model predicts a high CO* coverage under reaction conditions. The model is therefore self-consistent in CO* coverage.

Averaged over the experimental conditions, the model also predicts ~10^{-3} ML HCOO*, which has been suggested as a reaction intermediate by FTIR studies in the context of FA decomposition on Pd catalysts.[43, 73-79]

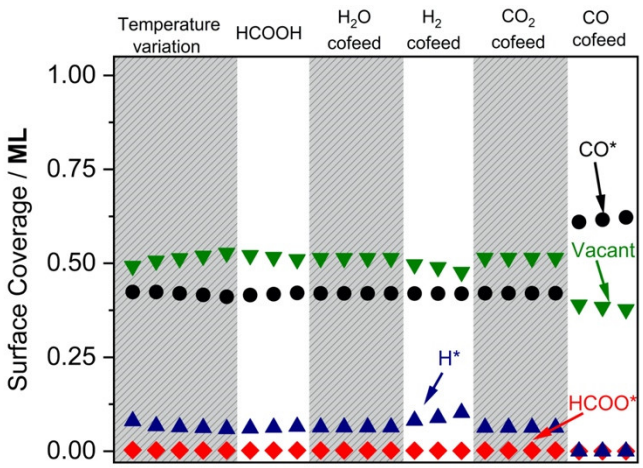

Figure 3 Coverages of relevant reaction intermediates under various experimental conditions, as predicted by the optimized CO* coverage cognizant Pd(100) model. Going from left to right, the shaded regions correspond to different experimental conditions (eg. variation in temperature, variation in the partial pressure of reactant/product, etc.). The experimental data points for various shaded regions, are listed in **Table S1** (Supporting Information): Variation in Temperature (#1-5), P(HCOOH) (#6-8), P(H_2O) (#9-12), P(H_2) (#13-15), P(CO_2) (#16-19) and P(CO) (#20-22). In each shaded region, going left to right indicates the increase in the value of the corresponding experimental parameter (i.e., temperature or partial pressure of the indicated gas-phase species), e.g., for the section labeled 'Temperature variation' moving left to right, i.e., #1-5 (Supporting Information – **Table S1**), indicates increase in temperature, with other experimental parameters held constant.

Based on the results from the CO* coverage cognizant Pd(100) model and the clean Pd(100) model (see section S2.1 of the Supporting Information), we envision the following reaction mechanism for the (100) facet. As the reaction begins on reduced catalyst, the (100) facet is free of reaction intermediates and resembles the clean (100) model, converting FA to CO_2 + H_2 via the direct COOH* dehydrogenation mechanism (HCOOH* ↔ HCOOH*pa** ↔ COOH* + H* ↔ CO_2* + 2H* ↔ CO_2 + H_2) and to CO + H_2O via the COOH* dehydroxylation mechanism (HCOOH* ↔

HCOOH*pa** ↔ COOH* + H* ↔ CO* + OH* + H* ↔ CO + H_2O) (see section S2.1 of the Supporting Information). Given the strong binding energy of CO* on clean Pd(100), CO* gradually accumulates on the (100) facet. As the CO* coverage increases to the steady-state value of ~4/9 ML, the COOH* dehydrogenation and dehydroxylation mechanisms, that carried the flux on clean (100), get destabilized due to the lateral adsorbate-adsorbate repulsions, rendering only the formate pathway (HCOOH* ↔ HCOO* + H* ↔ CO_2* + 2H* ↔ CO_2 + H_2), which is destabilized to a lesser extent, active under steady-state conditions, which remains selective toward FA dehydrogenation. In summary, our results suggest that under our examined reaction conditions the FA decomposition reaction on Pd(100) would occur through the HCOO* mechanism and that CO* would be the most abundant surface intermediate with a coverage of ~4/9 ML. Yet, the optimized CO* coverage-cognizant Pd(100) model failed to accurately rationalize the experimentally determined dehydration selectivity on Pd/C. Contrary to our experimental results on Pd/C, the Pd(100) model was found to be completely selective towards FA dehydrogenation and predicted no flux through the dehydration pathway. In addition, the model was unable to capture FA dehydrogenation TOFs under CO-cofeed conditions. We therefore conclude that Pd(100), by itself, fails to capture the active site for FA decomposition on Pd/C. However, since the model required small corrections to the DFT energetics to explain the dehydrogenation subset of the reaction kinetics experiments, we cannot disqualify the possibility that the Pd(100) facet potentially contributes towards a portion of the dehydrogenation flux, under certain reaction conditions.

CO* Coverage Cognizant Pd(111) Model

Upon parameter estimation, the model formulated using DFT energetics derived on the 5/9 ML CO*-covered Pd(111) yielded one solution that was able to rationalize our reaction kinetics

experimental results. The parity plots comparing the model-predicted TOFs with the respective experimental values (**Figure 4**) demonstrate a good fit with a mean absolute percentage error of 3.7% ($R^2 = 0.94$) and mean relative percentage error of 7.3% ($R^2 = 0.96$) for the dehydrogenation and dehydration pathways, respectively. Importantly, the model was able to capture the CO co-feed subset of the experimental dataset which was not captured by the clean Pd(100) model, the clean Pd(111) model, or the CO* coverage cognizant Pd(100) model.

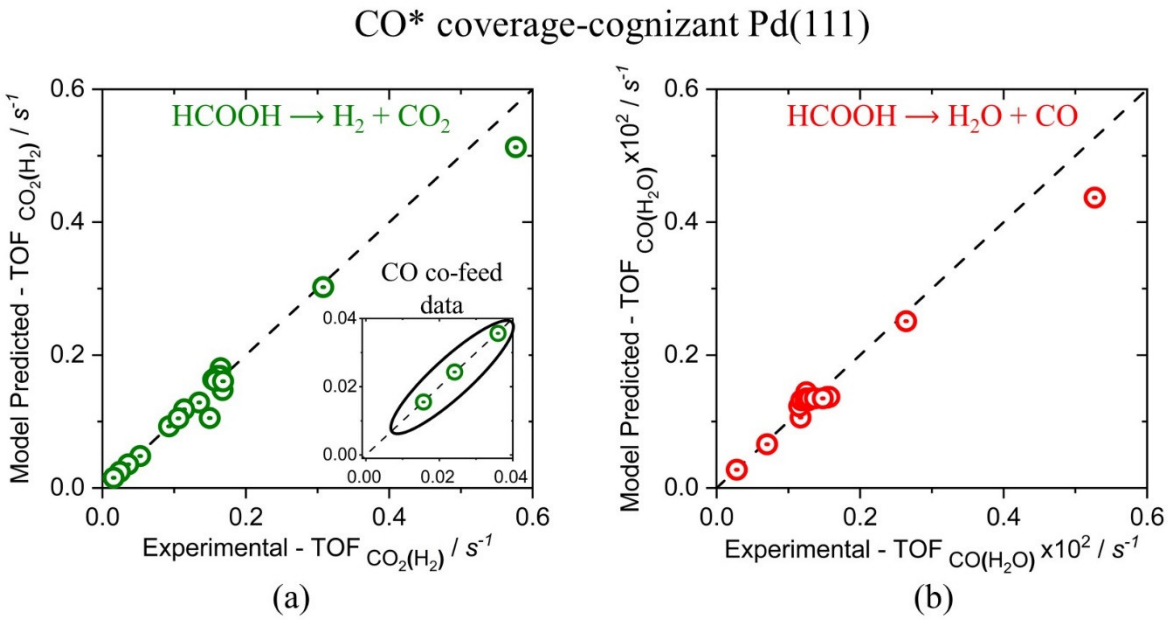

Figure 4 Parity plot of CO* coverage-cognizant Pd(111) model predicted vs. experimental TOFs (s^{-1}) for (a) Dehydrogenation: HCOOH ↔ CO_2 + H_2; inset shows the parity at low TOFs (corresponding to CO co-feed experiments), (b) Dehydration: HCOOH ↔ CO + H_2O.

To fit the experimental kinetics dataset, parameter estimation required adjusting the binding energy of closed-shell adsorbed intermediates, HCOOH* and HCOOH*pa**, by -0.27 and -0.16 eV, respectively (**Table 2**). We suggest that these corrections can be at least partly attributed to the lack of including dispersion effects in our PW91-GGA calculations.[68, 80] To the best our knowledge there are no studies reporting the experimentally determined binding energy of HCOOH* on

Pd(111) which could facilitate a direct comparison with the DFT computed binding energy. However, by comparing with the experimentally (single crystal adsorption calorimetry (SCAC)) reported binding energy of HCOOH* at low-coverage level (1/4 ML) on Pt(111) (BE = –0.37 eV)[81] and on Ni(111) (BE = –0.32 eV),[82] we determined that PW91-GGA using a computational setup consistent with the one used in this study,[83] systematically underpredicts the BE of HCOOH* by ~0.2-0.3 eV (see Table S16 in **Section S4 of** Supporting Information); this is similar in magnitude to the stabilization for HCOOH* predicted by our parameter estimation procedure. Parameter estimation requires correction in the binding energy of *cis*-COOH* by -0.09 eV, which is within DFT error. The binding energy of H* and CO* required destabilization by 0.15 and 0.34 eV (overall correction for CO*; including the correction of CO(g) energy – see **Section 2.2**), respectively. A benchmarking study by Wellendorff *et al.*, which compared the SCAC adsorption energies of chemisorbed species with those calculated with the PW91-GGA functional, revealed a systematic over-binding from theory.[68] Binding of CO* on clean Pd(111) required a destabilization of ~0.45 eV to match the SCAC values measured at low adsorbate coverages (1/4 ML).[84] Similarly, the reaction energy for dissociative adsorption of H_2 on Pd(111) was calculated as -1.09 eV compared to experimentally measured value of -0.91 eV[68] for 1/4 ML of adsorbed H*, which translates to PW91-GGA overpredicting the binding of each H* by 0.09 eV. Thus, the corrections to the adsorbed species binding energies, predicted by parameter estimation, are consistent with the intrinsic errors of PW91-GGA DFT calculations (Supporting Information – **Section S4**). In addition, this solution required three corrections for the activation energy barriers. The activation energy barrier for (1) dehydrogenation of HCOOH*pa** to form COOH* + H* required a correction of -0.19 eV, (2) H-H recombination to form H_2(g) required a correction of -0.20 eV, and (3)

dehydrogenation of COH* to form CO* + H* required a correction of +0.08 eV; all three corrections are within the typical DFT error (~0.2 eV).

Table 2 Corrections to the DFT-derived binding energy (ΔBE) of reaction intermediates and activation energy barrier (ΔE_A) of the elementary steps for the CO* coverage cognizant Pd(111) model, as obtained from parameter estimation. †For CO*, the number outside the parenthesis refers to the correction in the energy of CO* as predicted from parameter estimation, while the number within the parenthesis ([•]) represents the 'overall' correction in the binding energy of CO*, which also includes the adjustment to the CO(g) gas-phase energy by -0.60 eV (see Section 2.2 – Model Formulation).

5/9 ML CO-covered Pd(111)*	*Corrections / eV*
Intermediate	ΔBE
HCOOH*	-0.27
HCOOH*pa**	-0.16
cis-COOH*	-0.09
CO*	-0.26 [0.34]†
H*	+0.15
Elementary Step	ΔE_A
HCOOH*pa** + * ↔ COOH* + H*	-0.19
2H* ↔ H_2(g) + 2*	-0.20
COH* + * ↔ CO* + H*	+0.08

For the optimized CO* coverage cognizant Pd(111) solution, the flux goes entirely through the carboxyl (COOH*) mechanism (**Figure 5**). Under all experimental conditions, the dehydration reaction goes through the dehydroxylation of *cis*-COOH* (HCOOH* ↔ HCOOH*pa** ↔ COOH* + H* ↔ *cis*-COOH* + H* ↔ CO* + OH* + H* ↔ CO + H_2O). The dehydrogenation reaction occurs via two sub-mechanisms: (1) direct decomposition of COOH* (HCOOH* ↔ HCOOH*pa** ↔ COOH* + H* ↔ CO_2* + 2H* ↔ CO_2 + H_2) and (2) CO*-assisted decomposition of COOH* (HCOOH* (+**CO***) ↔ HCOOH*pa** (+**CO***) ↔ COOH* + H* (+**CO***) ↔ CO_2* + H* + **CO**H* ↔ CO_2* + 2H* (+**CO***) ↔ CO_2 + H_2 (+**CO***); whereby (+**CO***) denotes spectator CO*). In the CO*-assisted mechanism, COOH* transfers its H to a nearby spectator CO* to form COH*, which then dehydrogenates to release H* and regenerate the spectator CO*. At the baseline condition for our experiments (2.6% FA, 373 K), the CO*-assisted COOH* mechanism contributes ~40% of

the dehydrogenation flux, with the remainder accounted for by the direct COOH* decomposition mechanism. Interestingly, we find that under CO co-feed conditions (0.02-0.1% CO, 2.6% FA, 373 K) the direct COOH* decomposition mechanism becomes inactive and only the CO*-assisted COOH* mechanism contributes to the observed dehydrogenation flux, although the overall dehydrogenation TOF was reduced by a factor of 4-10 vs. the baseline conditions (2.6% FA, 373 K). The dehydration reaction order for the CO-cofeed experiments could not be accurately quantified due to small selectivity of Pd/C towards CO formation. Our CO* coverage cognizant model suggests that the dehydration TOF is reduced by a factor of c.a. 2-10 under the investigated CO co-feed partial pressures vs. the baseline conditions (2.6% FA, 373 K).

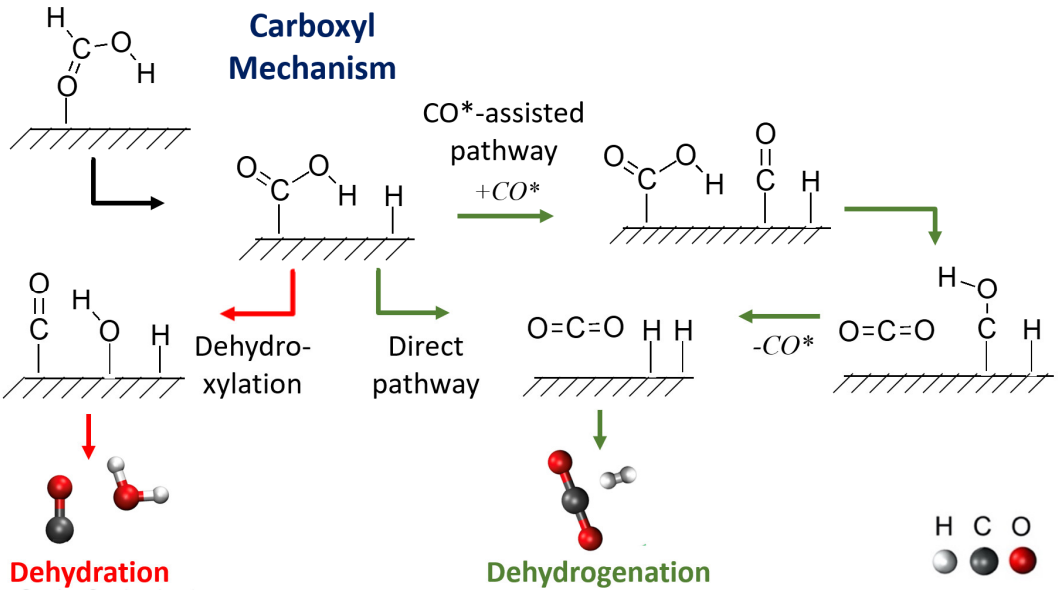

Figure 5 Simplified reaction mechanism for FA decomposition determined by the optimized CO* coverage cognizant Pd(111) model (isomerization steps are not explicitly shown). The arrows correspond to the elementary steps in the dehydrogenation (green) and dehydration (red) pathways, respectively. Elementary steps with participation of a spectator CO* are denoted by ±*CO** by the arrows.

At the baseline condition (2.6% FA, 373 K) and considering the entire reaction network (both dehydrogenation and dehydration), the calculated degree of rate control[85] (X_{RC}) for the

dehydrogenation pathway was distributed over three elementary steps: (1) COOH* ↔ CO_2* + H* (X_{RC} = 0.25), (2) COH* ↔ CO* + H* (X_{RC} = 0.24), and (3) H* + H* ↔ H_2(g) (X_{RC} = 0.23). Further, X_{RC} values determined by considering: (1) direct COOH* mechanism and (2) CO*-assisted COOH* mechanism, one-at-a-time, are provided in the Table S15 (Supporting Information – **Section 3**). Averaged over all experimental conditions, the optimized CO* coverage cognizant Pd(111) model predicts surface coverages of 0.34 ML CO*, 0.05 ML COH*, 0.02 ML H*, and 0.59 ML vacant sites (**Figure 6**). Consistent with the assumption of a partially CO*-covered Pd(111) surface at which the energetics for this model were derived with DFT, the optimized model suggests CO* as the most abundant surface intermediate. Although the model predicted CO* coverages were ~2/9 ML lower than the coverage of 5/9 ML that was explicitly considered in our DFT calculations, the inclusion of CO* coverage dependent thermochemistry and kinetics ensured the use of energetics that were consistent with the CO* coverages predicted by the microkinetic models.

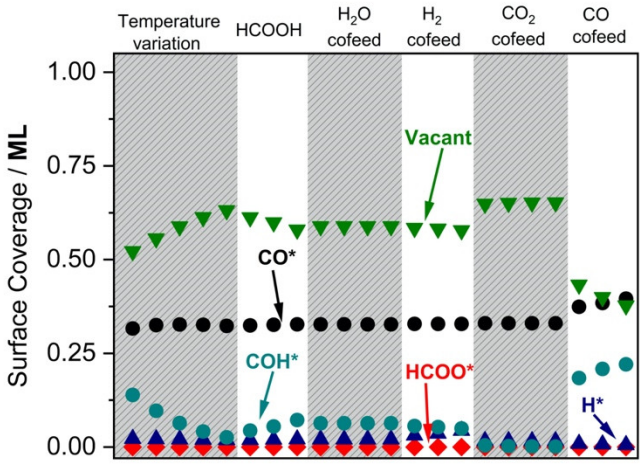

Figure 6 Coverages of relevant reaction intermediates under various experimental conditions, as predicted by the optimized CO* coverage cognizant Pd(111) model. Going from left to right, the shaded regions correspond to different experimental conditions (e.g., variation in temperature, variation in the partial pressure of reactant/product, etc.). The experimental data points for various shaded regions, are listed in **Table S1** (Supporting Information): Variation in Temperature (#1-5), P(HCOOH) (#6-8), P(H_2O) (#9-12), P(H_2) (#13-15), P(CO_2) (#16-19) and P(CO) (#20-22). In each shaded region, going left to right indicates the increase in the value of the corresponding experimental parameter (i.e., temperature or partial pressure

of the indicated gas-phase species), e.g., for the section labeled 'Temperature variation' moving left to right, i.e., #1-5 (Supporting Information – **Table S1**), indicates increase in temperature, with other experimental parameters held constant.

Inclusion of CO* coverage-dependent energetics and of spectator CO*-assisted mechanisms were essential for explaining the experimental kinetics, especially for the CO-cofeed subset of the experimental dataset (0.02-0.1% CO, 2.6% FA, 373 K). Under the CO-cofeed conditions, our models suggest that the coverage of CO* increased to ~0.4 ML compared with ~0.32 ML under the baseline conditions (2.6% FA, 373 K). This increase in CO* coverage leads to increased repulsive interactions between adsorbates and destabilizes the energetics for the direct COOH* dehydrogenation mechanism, rendering that decomposition mechanism inactive under the CO-cofeed conditions. The increased CO* coverage, however, enables the spectator CO*-assisted COOH* decomposition routes to contribute towards FA dehydrogenation under CO-cofeed conditions. Accordingly, our results suggest that inclusion of coverage effects, in particular the use of energetics cognizant with coverages of spectator species, and consideration of spectator-assisted mechanisms are critical for accurately capturing reaction kinetics experiments. Further, the model demonstrated close agreement with the experimentally determined apparent activation energy barriers and reaction orders, for both the dehydrogenation and dehydration pathways (

Table 3).

Table 3 Comparison of experimentally determined and model-predicted apparent activation energy barriers and reaction orders with respect to partial pressure of HCOOH, H_2O, H_2, CO_2 and CO for the dehydrogenation ($HCOOH \leftrightarrow CO_2 + H_2$) and dehydration pathway ($HCOOH \leftrightarrow CO + H_2O$) on the parameter adjusted CO* coverage cognizant Pd(111) model. †The dehydration reaction order for the CO-cofeed experiments could not be accurately quantified due to small selectivity of Pd/C towards CO formation.

CO* coverage-cognizant Pd(111) model	**Dehydrogenation**		**Dehydration**	
	Expt	**Model**	**Expt**	**Model**
E_A (kJ/mol)	69.0	68.2	82.9	79.4
HCOOH	-0.03	0.22	0.08	0.34
H_2O	-0.02	0.00	0.04	0.00

H_2	-0.26	-0.23	0.02	0.00
CO_2	-0.00	-0.02	0.11	0.00
CO	-0.58	-0.58	--†	--†

In summary, the optimized CO* coverage cognizant Pd(111) model was able to accurately capture the experimental reaction kinetics. The corrections to the DFT-derived activation energy barriers derived via parameter adjustments were within the typical DFT-GGA error of ~0.2 eV.[68, 69] Averaged over the experimental conditions, the model predicted CO* coverage of ~3/9 ML which was consistent with the assumption of a partially CO*-covered Pd(111), at which DFT energetics for this model were calculated. Our model is therefore, self-consistent with respect to CO* coverages. The reaction flux for both the dehydrogenation and dehydration pathways goes through the COOH* mechanism. Finally, our results suggest that a CO* spectator assisted COOH* mechanism plays a critical role in rationalizing the experimentally observed reaction fluxes, especially for the CO-cofeed experiments.

4. ACTIVE SITE FOR VAPOR-PHASE DECOMPOSITION OF FA ON PD/C

The optimized CO* coverage cognizant Pd(100) model failed to serve as an accurate model for the active site of FA decomposition on Pd/C. Although the model was self-consistent in terms of the CO* coverage and the corrections to the energetics were within the DFT error, it was unable to rationalize the experimental dataset, specifically on the following two counts: (1) Contrary to the experimentally determined selectivity of ~1% towards FA dehydration, the model predicted no flux through the dehydration pathway, under any experimental condition. Accordingly, the Pd(100) model failed to capture the selectivity towards the dehydration reaction. (2) The Pd(100) model predicted a complete shutdown of the dehydrogenation reaction under CO-cofeed conditions, which was in contrast to the reaction kinetics experimental results.

On the other hand, the optimized CO* coverage cognizant Pd(111) model was able to fit the entire experimental kinetics dataset (both the dehydrogenation and dehydration TOFs), and required corrections to the DFT energetics that were within the standard DFT error. Averaged over the experimental conditions, the model predicted coverage of ~1/3 ML CO* which was consistent with the assumption of a partially CO*-covered surface at which the DFT energetics for this model were calculated at.

From our results, and assuming that catalysis is carried by either the Pd(100) or the Pd(111) facets, we believe that the following two descriptions for the Pd/C nanoparticles are plausible, under the reaction conditions considered (**Figure 7**). (1) **Single-site model**: Wherein the Pd(111) facets of the nanoparticle are partially covered with CO* (~0.3 ML) and serve as the active site for FA decomposition, converting FA to H_2+CO_2 and H_2O+CO via the dehydrogenation and dehydration pathways, respectively. The reaction proceeds entirely via the spectroscopically elusive carboxyl (COOH*) intermediate. In this description of the Pd nanoparticles, the Pd(100) facets are largely poisoned by CO* (0.4-0.5 ML) and do not contribute toward FA decomposition (**Figure 7** (a)). (2) **Dual-site model**: Since the parameter-adjustment procedure led to corrections for both partially CO*-covered Pd(111) and Pd(100) models that were within the DFT error – we cannot exclude the possibility that both these facets contribute to FA decomposition (**Figure 7** (b)). In such a scenario, both Pd(100) and Pd(111) facets contribute to the dehydrogenation flux via the formate (HCOO*) and the carboxyl (COOH*) intermediate, respectively. However, since our results suggest that Pd(100) preferentially decomposes FA to H_2, only the Pd(111) facets would account for the dehydration flux (via COOH* dehydroxylation). Importantly, under CO-cofeed conditions, since Pd(100) was determined to be poisoned by CO* and was rendered inactive, only Pd(111) would contribute to the dehydrogenation flux. Although the dehydration flux could not be

experimentally quantified under CO-cofeed conditions, our results suggest that only Pd(111) will contribute toward the dehydration flux (via COOH* dehydroxylation). The dehydration TOFs were reduced by a factor of 2-10 under the CO-cofeed conditions vs. the baseline condition (2.6% FA, 373 K).

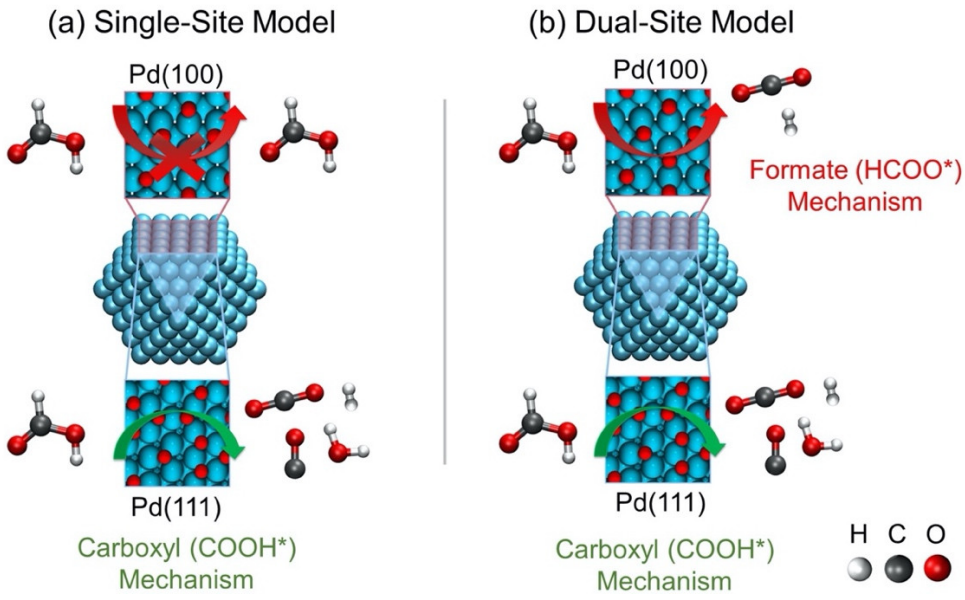

Figure 7 Facet-dependent contributions to FA decomposition over idealized Pd/C nanoparticles: (a) Single-site model – partially (~0.3 ML) CO*-covered Pd(111) facet serving as the active site and partially (0.4-0.5 ML) CO*-covered Pd(100) poisoned under reaction conditions, (b) Dual-site model – both partially CO*-covered (~0.3 ML) Pd(111) and (~0.4-0.5 ML) Pd(100) are active towards FA decomposition, with Pd(100) active only for FA dehydrogenation. Nature of the reactive-intermediate (carboxyl vs. formate) carrying the reaction flux, as determined from the optimized microkinetic models, is indicated next to the respective facets. Color code for atoms: white – H, red – O, dark gray – C, and blue – Pd.

Advances in characterization techniques such as high-resolution transmission electron microscopy (HRTEM) and diffuse reflectance Fourier transform infrared (FT-IR) spectroscopy (DRIFTS), in conjunction with first principles DFT modeling can help determine the statistical distribution of the sites present on a nanoparticle catalyst sample. Additionally, determination of the intrinsic catalytic activity of various facets, by performing reaction kinetics experiments on shape-selective

catalyst nanoparticles, which preferentially expose a certain facet, e.g., nanocubes or octahedral nanoparticles that preferentially expose the (100) or (111) facet, respectively, can potentially help deconvolute flux contribution from various site types even further.

5. CONCLUSION

A combination of DFT-informed mean-field microkinetic models and reaction kinetics experiments were utilized to gain an in-depth understanding of FA decomposition catalyzed by Pd/C. Upon parameter estimation for capturing the experimental data, the microkinetic models formulated using DFT energetics on clean Pd(100) and Pd(111) required large corrections of the DFT energetics and were unable to rationalize the entire experimental dataset. Inconsistent with the assumption of clean surface used in the DFT calculations, these models predicted high CO* coverage (~0.99 ML and ~0.90 ML for Pd(100) and Pd(111), respectively). Accordingly, we reformulated microkinetic models using DFT energetics that were calculated on partially (5/9 ML) CO*-covered Pd(100) and Pd(111) facets, which explicitly account for the presence of CO* on the catalyst surface. CO* coverage-dependent energetics were incorporated in our models, which were derived by calculating the reaction thermochemistry and kinetics at varying coverages of CO* spectators. Upon parameter estimation, these revised models predicted surface coverages that were consistent with the coverage of CO* at which the DFT calculations were performed, i.e., the models were CO* coverage self-consistent. The partially (~0.4 ML) CO*-covered Pd(100) model was able to rationalize only a subset of the dehydrogenation TOFs, but was unable to explain the experimentally observed selectivity towards the dehydration reaction. Importantly, a partially (~0.3 ML) CO*-covered Pd(111) was able to explain the entire experimental dataset (both dehydrogenation and dehydration TOFs), including the CO-cofeed subset which could not be explained by the other models. The reaction on the partially CO*-covered Pd(111) model occurs

through the carboxyl (COOH*) mechanism, with both the direct and CO*-assisted COOH* mechanisms contributing to FA dehydrogenation. Importantly, the CO*-assisted COOH* mechanism plays a critical in rationalizing the dehydrogenation TOFs, especially under the CO-cofeed conditions.

Our results demonstrate that a partially CO*-covered Pd(111) model is capable of rationalizing the experimental activity and selectivity, and can therefore, by itself, serve as an accurate description for the active site for FA decomposition on Pd/C catalysts. However, since the optimized CO* coverage cognizant Pd(100) model (requiring small corrections) is able to fit the dehydrogenation TOFs for all but the CO-cofeed conditions, we cannot exclude the possibility that Pd(100) might also contribute towards a portion of the dehydrogenation flux under conditions except for the CO cofeed conditions.

Our study demonstrates the complexity of deciphering the *in situ* nature of the active site for heterogeneously catalyzed reactions and the importance of computational models for developing a more realistic description of the active site, i.e., including spectator coverage effects and spectator-assisted mechanisms. Detailed atomic-scale mechanistic insights derived from this work could be valuable for designing improved catalytic materials that are more active and selective than monometallic catalysts, thereby further enabling FA as a promising hydrogen storage material.

COMPETING INTERESTS

The authors declare no competing interests.

SUPPORTING INFORMATION

Experimental data, details regarding model formulation, and energetics parameters for formulating mean-field microkinetic models. (PDF)

DACAPO .nc files for converged structures. (ZIP)

ACKNOWLEDGMENTS

This work was supported by the U.S. Department of Energy (DOE)–Basic Energy Sciences (BES), Office of Chemical Sciences, Catalysis Science program, grant DE-FG02-05ER15731. The calculations were performed at supercomputing centers located at the National Energy Research Scientific Computing Center, supported by DOE contract DE-AC02-05CH11231, and at the Center for Nanoscale Materials at Argonne National Laboratory, supported by DOE contract DE-AC02-06CH11357. We thank Dr. Madelyn R. Ball for STEM characterization of the catalysts. We also thank Dr. Lang Xu and Dr. Benjamin Chen for insightful comments on the manuscript, and Dr. Anthony Plauck and Dr. Isaias Barbosa Aragão for helpful discussions.

REFERENCES

1. Alonso, D. M.,Bond, J. Q.,Dumesic, J. A., Catalytic conversion of biomass to biofuels. *Green Chemistry* **2010,** *12* (9), 1493-1513.
2. Deng, L.,Li, J.,Lai, D. M.,Fu, Y.,Guo, Q. X., Catalytic conversion of biomass-derived carbohydrates into γ-valerolactone without using an external H2 supply. *Angewandte Chemie - International Edition* **2009,** *48* (35), 6529-6532.
3. Bozell, J. J.,Petersen, G. R., Technology development for the production of biobased products from biorefinery carbohydrates—the US Department of Energy's "Top 10" revisited. *Green Chemistry* **2010,** *12* (4), 539-554.
4. Johnson, T. C.,Morris, D. J.,Wills, M., Hydrogen generation from formic acid and alcohols using homogeneous catalysts. *Chemical Society Reviews* **2010,** *39* (1), 81-88.
5. Laurenczy, G.,Dyson, P. J., Homogeneous catalytic Dehydrogenation of formic acid: Progress towards a Hydrogen-based economy. *Journal of the Brazilian Chemical Society* **2014,** *25* (12), 2157-2163.
6. Mellmann, D.,Sponholz, P.,Junge, H.,Beller, M., Formic acid as a hydrogen storage material – development of homogeneous catalysts for selective hydrogen release. *Chem. Soc. Rev.* **2016,** *45* (14), 3954-3988.

7. Grasemann, M.,Laurenczy, G., Formic acid as a hydrogen source – recent developments and future trends. *Energy & Environmental Science* **2012,** *5*, 8171-8181.
8. Singh, A. K.,Singh, S.,Kumar, A., Hydrogen energy future with formic acid: a renewable chemical hydrogen storage system. *Catal. Sci. Technol.* **2015,** *6*, 12-40.
9. Czaun, M.,Goeppert, A.,May, R.,Haiges, R.,Prakash, G. K. S.,Olah, G. A., Hydrogen generation from formic acid decomposition by ruthenium carbonyl complexes. Tetraruthenium dodecacarbonyl tetrahydride as an active intermediate. *ChemSusChem* **2011,** *4* (9), 1241-1248.
10. Enthaler, S.,von Langermann, J.,Schmidt, T., Carbon dioxide and formic acid—the couple for environmental-friendly hydrogen storage? *Energy & Environmental Science* **2010,** *3* (9), 1207-1207.
11. Yu, X.,Pickup, P. G., Recent advances in direct formic acid fuel cells (DFAFC). 2008; Vol. 182, pp 124-132.
12. El-Nagar, G. A.,Hassan, M. A.,Lauermann, I.,Roth, C., Efficient Direct Formic Acid Fuel Cells (DFAFCs) Anode Derived from Seafood waste: Migration Mechanism. *Scientific Reports* **2017,** *7* (1), 1-11.
13. El-Nagar, G. A.,Darweesh, A. F.,Sadiek, I., A novel nano-palladium complex anode for formic acid electro-oxidation. *Electrochimica Acta* **2016,** *215*, 334-338.
14. Rice, C.,Ha, S.,Masel, R. I.,Waszczuk, P.,Wieckowski, A.,Barnard, T., Direct formic acid fuel cells. *Journal of Power Sources* **2002,** *111* (1), 83-89.
15. Jiang, K.,Zhang, H.-X.,Zou, S.,Cai, W.-B., Electrocatalysis of formic acid on palladium and platinum surfaces: from fundamental mechanisms to fuel cell applications. *Phys. Chem. Chem. Phys.* **2014,** *16* (38), 20360-20376.
16. Rice, C. A.,Bauskar, A.,Pickup, P. G., *Recent advances in electrocatalysis of Formic acid oxidation*. Electrocatalysis in fuel cells: 2013; Vol. 9, p 69-87.
17. Rahimi, A.,Ulbrich, A.,Coon, J. J.,Stahl, S. S., Formic-acid-induced depolymerization of oxidized lignin to aromatics. *Nature* **2014,** *515* (7526), 249-252.
18. Wang, L.,Zhang, B.,Meng, X.,Su, D. S.,Xiao, F. S., Hydrogenation of biofuels with formic acid over a palladium-based ternary catalyst with two types of active sites. *ChemSusChem* **2014,** *7* (6), 1537-1541.
19. Gilkey, M. J.,Xu, B., Heterogeneous Catalytic Transfer Hydrogenation as an Effective Pathway in Biomass Upgrading. 2016; Vol. 6, pp 1420-1436.
20. Singh, A. K.,Jang, S.,Kim, J. Y.,Sharma, S.,Basavaraju, K. C.,Kim, M. G.,Kim, K. R.,Lee, J. S.,Lee, H. H.,Kim, D. P., One-Pot Defunctionalization of Lignin-Derived Compounds by Dual-Functional Pd50Ag50/Fe3O4/N-rGO Catalyst. *ACS Catalysis* **2015,** *5* (11), 6964-6972.
21. Feng, J.,Gu, X.,Xue, Y.,Han, Y.,Lu, X., Production of γ-valerolactone from levulinic acid over a Ru/C catalyst using formic acid as the sole hydrogen source. *Science of the Total Environment* **2018,** *633*, 426-432.
22. Gao, Y.,Zhang, H.,Han, A.,Wang, J.,Tan, H. R.,Tok, E. S.,Jaenicke, S.,Chuah, G. K., Ru/ZrO2Catalysts for Transfer Hydrogenation of Levulinic Acid with Formic Acid/Formate Mixtures: Importance of Support Stability. *ChemistrySelect* **2018,** *3* (5), 1343-1351.
23. Hu, Z.,Tan, S.,Mi, R.,Li, X.,Bai, J.,Guo, X.,Hu, G.,Hang, P.,Li, J.,Li, D.,Yang, Y.,Yan, X., Formic Acid or Formate Derivatives as the In Situ Hydrogen Source in Au-Catalyzed Reduction of para -Chloronitrobenzene. *ChemistrySelect* **2018,** *3* (10), 2850-2853.
24. Ruppert, A. M.,Jędrzejczyk, M.,Sneka-Płatek, O.,Keller, N.,Dumon, A. S.,Michel, C.,Sautet, P.,Grams, J., Ru catalysts for levulinic acid hydrogenation with formic acid as a hydrogen source. *Green Chem.* **2016,** *18* (7), 2014-2028.

25. Ashokraju, M.,Mohan, V.,Murali, K.,Rao, M. V.,Raju, B. D.,Rao, K. S. R., Formic acid assisted hydrogenation of levulinic acid to γ -valerolactone over ordered mesoporous Cu/Fe2O3catalyst prepared by hard template method. *Journal of Chemical Sciences* **2018,** *130* (2), 1-8.
26. Lomate, S.,Sultana, A.,Fujitani, T., Vapor Phase Catalytic Transfer Hydrogenation (CTH) of Levulinic Acid to γ-Valerolactone Over Copper Supported Catalysts Using Formic Acid as Hydrogen Source. *Catalysis Letters* **2018,** *148* (1), 348-358.
27. Tedsree, K.,Li, T.,Jones, S.,Chan, C. W. A.,Yu, K. M. K.,Bagot, P. A. J.,Marquis, E. A.,Smith, G. D. W.,Tsang, S. C. E., Hydrogen production from formic acid decomposition at room temperature using a Ag–Pd core–shell nanocatalyst. *Nature Nanotechnology* **2011,** *6* (5), 302-307.
28. Bulushev, D. A.,Beloshapkin, S.,Ross, J. R. H., Hydrogen from formic acid decomposition over Pd and Au catalysts. *Catalysis Today* **2010,** *154* (1-2), 7-12.
29. Columbia, M. R.,Thiel, P. a., The interaction of formic acid with transition metal surfaces, studied in ultrahigh vacuum. *Journal of Electroanalytical Chemistry* **1994,** *369* (1-2), 1-14.
30. Yu, W. Y.,Mullen, G. M.,Flaherty, D. W.,Mullins, C. B., Selective hydrogen production from formic acid decomposition on Pd-Au bimetallic surfaces. *Journal of the American Chemical Society* **2014,** *136* (31), 11070-11078.
31. Larsson, R.,Jamróz, M. H.,Borowiak, M. A., On the catalytic decomposition of formic acid. I. The activation energies for oxide catalysis. *Journal of Molecular Catalysis A: Chemical* **1998,** *129* (1), 41-51.
32. Senanayake, S. D.,Mullins, D. R., Redox pathways for HCOOH decomposition over CeO2 surfaces. *Journal of Physical Chemistry C* **2008,** *112* (26), 9744-9752.
33. Peng, X. D.,Barteau, M. A., Dehydration of carboxylic acids on the MgO(100) surface. *Catalysis Letters* **1990,** *7* (5-6), 395-402.
34. Trillo, J. M.,Munuera, G.,Criado, J. M., Catalytic Decomposition of Formic Acid on Metal Oxides. *Catalysis Reviews* **1972,** *7* (1), 51-86.
35. Flaherty, D. W.,Berglund, S. P.,Mullins, C. B., Selective decomposition of formic acid on molybdenum carbide: A new reaction pathway. *Journal of Catalysis* **2010,** *269* (1), 33-43.
36. Koos, A.,Solymosi, F., Production of CO-free H2 by formic acid decomposition over Mo2C/carbon catalysts. *Catalysis Letters* **2010,** *138* (1-2), 23-27.
37. Grabow, L. C.,Gokhale, A. A.,Evans, S. T.,Dumesic, J. A.,Mavrikakis, M., Mechanism of the water gas shift reaction on Pt: First principles, experiments, and microkinetic modeling. *Journal of Physical Chemistry C* **2008,** *112* (12), 4608-4617.
38. Gokhale, A. A.,Dumesic, J. A.,Mavrikakis, M., Article On the Mechanism of Low-Temperature Water Gas Shift Reaction on Copper On the Mechanism of Low-Temperature Water Gas Shift Reaction on Copper. *J. Am. Chem. Soc.* **2008,** *130* (33), 1402-1414.
39. Zacharska, A. M.,Bulusheva, L.,Lisitsyn, A.,Beloshapkin, S.,Guo, Y.,Chuvilin, A.,Podyacheva, O.,Leahy, J.,Bulushev, D.,Zacharska, M.,Bulusheva, L. G.,Lisitsyn, A. S.,Beloshapkin, S., Factors influencing the performance of Pd / C catalysts in the green production of hydrogen from formic acid.
40. Bulushev, D. a.,Jia, L.,Beloshapkin, S.,Ross, J. R. H., Improved hydrogen production from formic acid on a Pd/C catalyst doped by potassium. *Chemical Communications* **2012,** *48* (35), 4184-4186.
41. Sachtler, W. M. H.,Fahrenfort, J. In *The catalytic decomposition of formic acid vapour on metals*, Paris (France), 1960; Paris (France), pp 831-831.

42. Tang, Y.,Roberts, C. A.,Perkins, R. T.,Wachs, I. E., Revisiting formic acid decomposition on metallic powder catalysts: Exploding the HCOOH decomposition volcano curve. *Surface Science* **2016,** *650*, 103-110.
43. Solymosi, F.,Koós, Á.,Liliom, N.,Ugrai, I., Production of CO-free H2 from formic acid. A comparative study of the catalytic behavior of Pt metals on a carbon support. *Journal of Catalysis* **2011,** *279* (1), 213-219.
44. Li, J.,Chen, W.,Zhao, H.,Zheng, X.,Wu, L.,Pan, H.,Zhu, J.,Chen, Y.,Lu, J., Size-dependent catalytic activity over carbon-supported palladium nanoparticles in dehydrogenation of formic acid. *Journal of Catalysis* **2017,** *352*, 371-381.
45. Navlani-García, M.,Mori, K.,Wen, M.,Kuwahara, Y.,Yamashita, H., Size effect of carbon-supported pd nanoparticles in the hydrogen production from formic acid. *Bulletin of the Chemical Society of Japan* **2015,** *88* (10), 1500-1502.
46. Madon, R. J.,Braden, D.,Kandoi, S.,Nagel, P.,Mavrikakis, M.,Dumesic, J. A., Microkinetic analysis and mechanism of the water gas shift reaction over copper catalysts. *Journal of Catalysis* **2011,** *281* (1), 1-11.
47. Bhandari, S.,Rangarajan, S.,Mavrikakis, M., Combining computational modeling with reaction kinetics experiments for elucidating the in situ nature of the active site in catalysis. *Accounts of Chemical Research* **2020,** *53* (9), 1893-1904.
48. Singh, S.,Li, S.,Carrasquillo-Flores, R.,Alba-Rubio, A. C.,Dumesic, J. A.,Mavrikakis, M., Formic Acid Decomposition on Au Catalysts: DFT, Microkinetic Modeling, and Reaction Kinetics Experiments. *AIChE Journal* **2014,** *60* (4), 1303-1319.
49. Plauck, A.,Stangland, E. E.,Dumesic, J. A.,Mavrikakis, M., Active sites and mechanisms for H_2O_2 decomposition over Pd catalysts. *Proceedings of the National Academy of Sciences of the United States of America* **2016,** *113* (14), E1973-82.
50. Wang, S.,Vorotnikov, V.,Vlachos, D. G., Coverage-Induced Conformational Effects on Activity and Selectivity: Hydrogenation and Decarbonylation of Furfural on Pd(111). *ACS Catalysis* **2015,** *5* (1), 104-112.
51. Bhandari, S.,Rangarajan, S.,Maravelias, C. T.,Dumesic, J. A.,Mavrikakis, M., Reaction Mechanism of Vapor-Phase Formic Acid Decomposition over Platinum Catalysts: DFT, Reaction Kinetics Experiments, and Microkinetic Modeling. *ACS Catalysis* **2020,** *10* (7), 4112-4126.
52. Rebarchik, M.,Bhandari, S.,Kropp, T.,Mavrikakis, M., How noninnocent spectator species improve the oxygen reduction activity of single-atom catalysts: Microkinetic models from first-principles calculations. *Acs Catalysis* **2020,** *10* (16), 9129-9135.
53. Chen, B. W.,Bhandari, S.,Mavrikakis, M., Role of Hydrogen-bonded Bimolecular Formic Acid–Formate Complexes for Formic Acid Decomposition on Copper: A Combined First-Principles and Microkinetic Modeling Study. *ACS Catalysis* **2021,** *11* (7), 4349-4361.
54. Stakheev, A. Y.,Mashkovskii, I.,Tkachenko, O.,Klementiev, K.,Grünert, W.,Baeva, G.,Kustov, L., Formation of palladium hydride nanoparticles in Pd/C catalyst as evidenced by in situ XAS data. *Russian Chemical Bulletin* **2009,** *58* (2), 280-283.
55. Knapton, A., Palladium alloys for hydrogen diffusion membranes. *Platinum Metals Review* **1977,** *21* (2), 44-50.
56. Spiewak, B. E.,Shen, J.,Dumesic, J. A., Microcalorimetric studies of CO and H2 adsorption on nickel powders promoted with potassium and cesium. *Journal of Physical Chemistry* **1995,** *99* (49), 17640-17644.
57. Zou, W.,Gonzalez, R. D., The preparation of silica supported Pd catalysts: the effect of pretreatment variables on particle size. *Catalysis Letters* **1992,** *12* (1-3), 73-86.

58. Perdew, J. P.,Chevary, J. A.,Vosko, S. H.,Jackson, K. A.,Pederson, M. R.,Singh, D. J.,Fiolhais, C., Atoms, molecules, solids, and surfaces: Applications of the generalized gradient approximation for exchange and correlation. *Physical Review B* **1992,** *46* (11), 6671-6687.
59. Hammer, B.,Hansen, L. B.,Nørskov, J. K., Improved adsorption energetics within density-functional theory using revised Perdew-Burke-Ernzerhof functionals. *Physical Review B - Condensed Matter and Materials Physics* **1999,** *59* (11), 7413-7421.
60. Greeley, J.,Nørskov, J. K.,Mavrikakis, M., Electronic Structure and Catalysis on Metal Surfaces. *Annual Review of Physical Chemistry* **2002,** *53* (1), 319-348.
61. Li, S.,Rangarajan, S.,Scaranto, J.,Mavrikakis, M., On the structure sensitivity of and CO coverage effects on formic acid decomposition on Pd surfaces. *Surface Science* **2021,** *709*, 121846.
62. Grabow, L. C.,Mavrikakis, M., Mechanism of methanol synthesis on cu through CO2 and CO hydrogenation. *ACS Catalysis* **2011,** *1* (4), 365-384.
63. Rangarajan, S.,Maravelias, C. T.,Mavrikakis, M., Sequential-Optimization-Based Framework for Robust Modeling and Design of Heterogeneous Catalytic Systems. *Journal of Physical Chemistry C* **2017,** *121* (46), 25847-25863.
64. Linstrom PJ, Mallard WG (2017) NIST Chemistry WebBook, NIST Standard Reference Database Number 69. https://webbook.nist.gov/chemistry/ (Accessed - 01/20/2023).
65. Hess, F.,Over, H., Kinetic Monte Carlo simulations of heterogeneously catalyzed oxidation reactions. *Catalysis Science and Technology* **2014,** *4* (3), 583-598.
66. Zhou, X.,Huang, Y.,Xing, W.,Liu, C.,Liao, J.,Lu, T., High-quality hydrogen from the catalyzed decomposition of formic acid by Pd-Au/C and Pd-Ag/C. *Chemical communications (Cambridge, England)* **2008,** (30), 3540-3542.
67. Ruthven, D. M.,Upadhye, R. S., The catalytic decomposition of aqueous formic acid over suspended palladium catalysts. *Journal of Catalysis* **1971,** *21* (1), 39-47.
68. Wellendorff, J.,Silbaugh, T. L.,Garcia-Pintos, D.,Nørskov, J. K.,Bligaard, T.,Studt, F.,Campbell, C. T., A benchmark database for adsorption bond energies to transition metal surfaces and comparison to selected DFT functionals. *Surface Science* **2015,** *640*, 36-44.
69. Matera, S.,Schneider, W. F.,Heyden, A.,Savara, A., Progress in Accurate Chemical Kinetic Modeling, Simulations, and Parameter Estimation for Heterogeneous Catalysis. *ACS Catalysis* **2019,** *9* (8), 6624-6647.
70. Xu, P.,Bernal-Juan, F. D.,Lefferts, L., Effect of oxygen on formic acid decomposition over Pd catalyst. *Journal of catalysis* **2021,** *394*, 342-352.
71. Jiang, K.,Xu, K.,Zou, S.,Cai, W.-B., B-Doped Pd catalyst: boosting room-temperature hydrogen production from formic acid–formate solutions. *Journal of the American chemical society* **2014,** *136* (13), 4861-4864.
72. Zhou, Y.-W.,Chen, Y.-F.,Qin, X.,Jiang, K.,Lin, W.-F.,Cai, W.-B., Boosting electrocatalytic oxidation of formic acid on SnO2-decorated Pd nanosheets. *Journal of Catalysis* **2021,** *399*, 8-14.
73. Cabilla, G.,Bonivardi, A. L.,Baltanás, M. A., Infrared study of the adsorption of formic acid on clean and Ca-promoted Pd/SiO2 catalysts. *Applied Catalysis A: General* **2003,** *255* (2), 181-195.
74. Aas, N.,Li, Y.,Bowker, M., The adsorption and decomposition of formic acid on clean and oxygen-dosed Pd(110). *Journal of Physics: Condensed Matter* **1991,** *281* (110).
75. Zheng, T.,Stacchiola, D.,Saldin, D. K.,James, J.,Sholl, D. S.,Tysoe, W. T., The structure of formate species on Pd(111) calculated by density functional theory and determined using low energy electron diffraction. *Surface Science* **2005,** *574* (2-3), 166-174.

76. Davis, J. L.,Barteau, M. A., Reactions of carboxylic acids on the Pd(111)-(2 × 2)O surface: multiple roles of surface oxygen atoms. *Surface Science* **1991,** *256* (1-2), 50-66.
77. Egawa, C.,Doi, I.,Naito, S.,Tamaru, K., Adsorption of Methanol, Formaldehyde and Formic Acid on Pd(100) Surfaces Modified By A Sodium and Sodium Oxide Overlayer. **1986,** *176*, 491-504.
78. Jorgensen, S. W.,Madix, R. J., Active oxygen on group VIII metals: Activation of formic acid and formaldehyde on Pd(100). *Journal of the American Chemical Society* **1988,** *110* (2), 397-400.
79. Jeroro, E.,Vohs, J. M., Reaction of formic acid on Zn-modified Pd(111). *Catalysis Letters* **2009,** *130* (3-4), 271-277.
80. Sauer, J.,Ugliengo, P.,Garrone, E.,Saunders, V. R., Theoretical Study of van der Waals Complexes at Surface Sites in Comparison with the Experiment. *Chemical Reviews (Washington, DC, United States)* **1994,** *94* (7), 2095-2160.
81. Silbaugh, T. L.,Karp, E. M.,Campbell, C. T., Energetics of methanol and formic acid oxidation on Pt(111): Mechanistic insights from adsorption calorimetry. *Surface Science* **2016,** *650*, 140-143.
82. Zhao, W.,Carey, S. J.,Morgan, S. E.,Campbell, C. T., Energetics of adsorbed formate and formic acid on Ni(111) by calorimetry. *Journal of Catalysis* **2017,** *352*, 300-304.
83. Herron, A.,Scaranto, J.,Ferrin, P.,Li, S.,Mavrikakis, M., Trends in Formic Acid Decomposition on Model Transition Metal Surfaces : A Density Functional Theory study. *ACS Catalysis* **2014,** *4* (0001), 4434-4445.
84. Conrad, H.,Ertl, G.,Koch, J.,Latta, E. E., Adsorption of CO on Pd single crystal surfaces. *Surface Science* **1974,** *43* (2), 462-480.
85. Campbell, C. T., Finding the rate-determining step in a mechanism: Comparing DeDonder relations with the "Degree of Rate Control". *Journal of Catalysis* **2001,** *204* (2), 520-524.

For Table of Contents Only